Electronic Supplementary Material (ESI) for Nanoscale.
This journal is © The Royal Society of Chemistry 2021

Supporting Information

Ultrathin memristor based on two-dimensional WS_2/MoS_2 heterojunction

*Wenguang Zhang‡, Hui Gao‡, Chunsan Deng, Ting Lv, Sanlue Hu, Hao Wu, Songyan Xue, Yufeng Tao, Leimin Deng, Wei Xiong**

Wuhan National Laboratory for Optoelectronics, School of Optical and Electronic Information, Huazhong University of Science and Technology, Wuhan 430074, China.

*E-mail: weixiong@hust.edu.cn

1. Device fabrication

In this experiment, we use solid-state sulfurization to grow 2D material single layer and heterojunction. Molybdenum (purity: 99.99%) and tungsten (purity: 99.99%) sputtering target, and sulfur powder (purity: 99.9999%) are purchased from Sigma-Aldrich Chemical Company. All materials are used without further purification. First, we evenly coat the ultra-clean substrate with W and Mo metal atomic films at a rate of 5 Å s^{-1} by magnetron sputtering (Beijing WSP3200). We put the reacted precursor sulfur powder and the metal-plated sample in the rapid annealing furnace (MTI OFT-1200X), as shown in Figure S1a. The whole heating process is divided into three steps: first, the temperature in the furnace is increased from room temperature to 120 °C, and the Ar/H_2 mixed gas is continuously introduced at a low speed; second, the temperature in the furnace is increased to the designated sulfurization temperature (from 550 to 850 °C) after 30 minutes, and the temperature is maintained for 15 minutes; finally, we continuously pass in high-purity Ar during the cooling process. We can summarize the entire 2D material growth process into two

steps in Figure S1b, including metal deposition on various substrates and vacuum sulfurization. The top electrode of the 2D material memristor was deposited by e-beam evaporation (ALPHA-PLUSCO.Ltd, Ebeam-500s) at the rate of 2 Å s^{-1}.

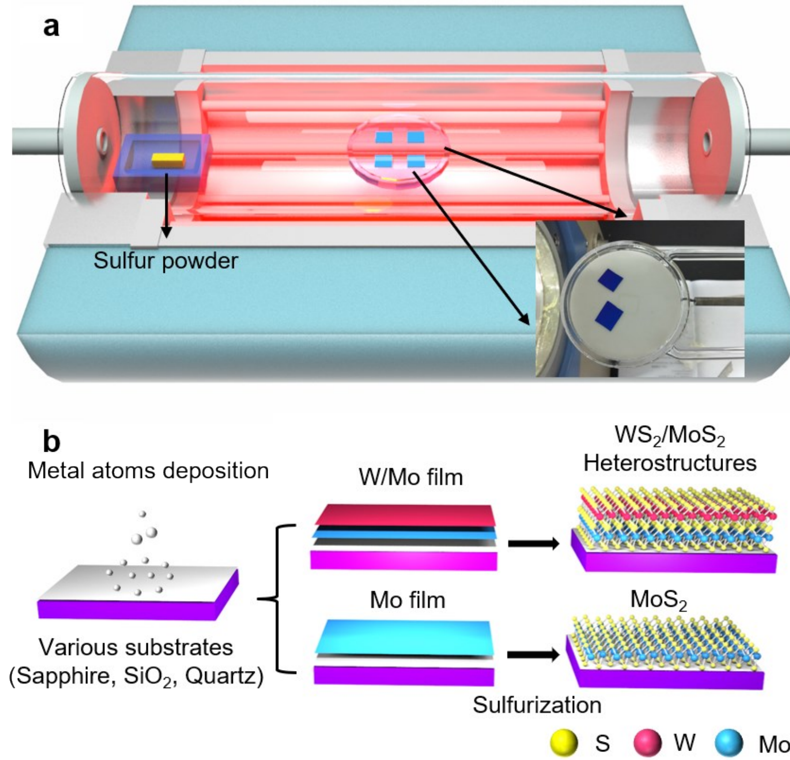

Figure S1. Diagrams of the synthesis of WS_2/MoS_2 heterojunction. (a) Schematics of the sulfurization furnace. (b) Schematics of metal deposition and sulfurization processes of the 2D materials.

2. AFM, Optical, and SEM Characterization of 2D materials

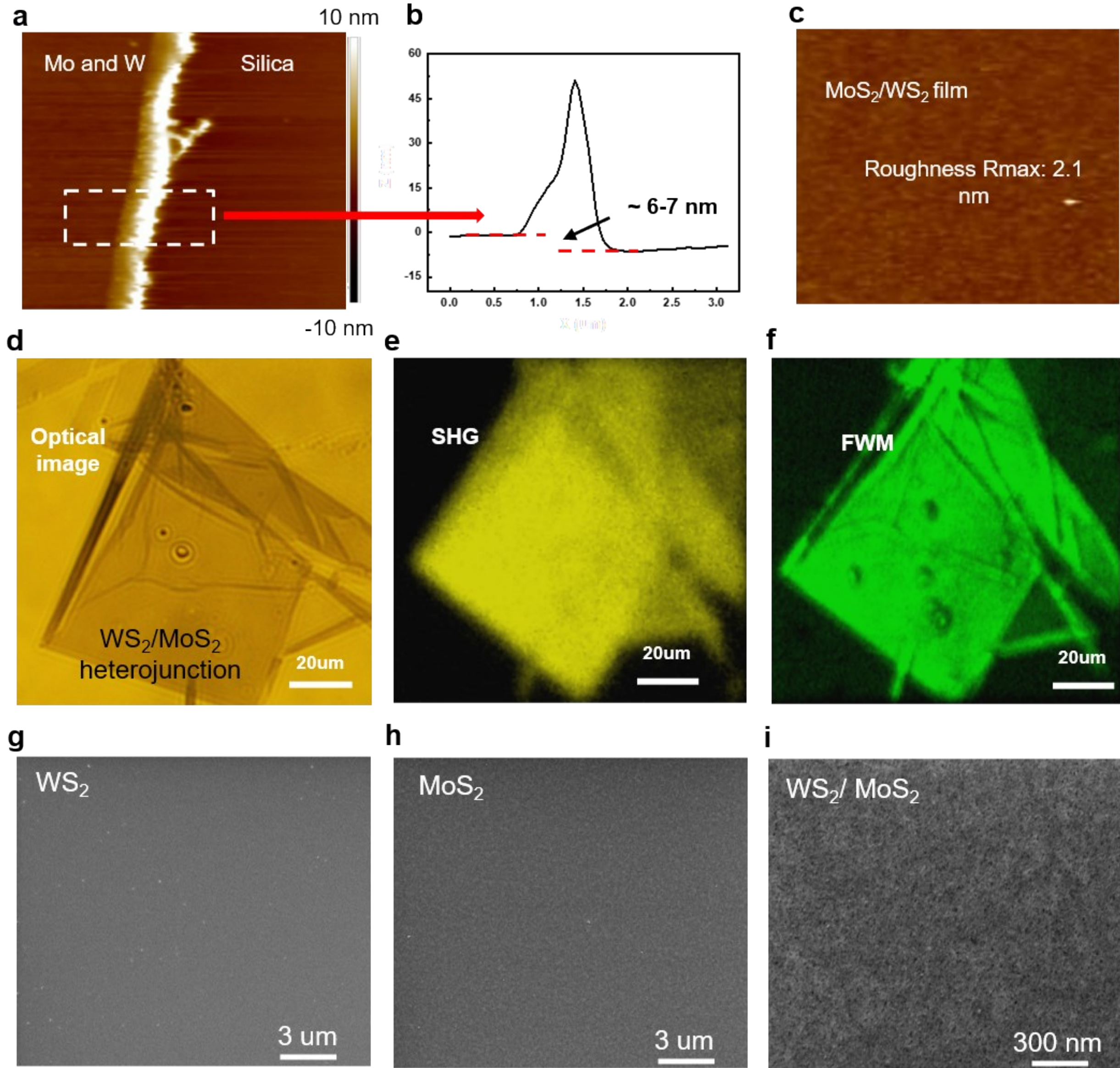

Figure S2. Characterization of the metal thin films of W and Mo before and after sulfurization. (a,b) AFM characterization results of the sample before sulfurization; (c) AFM characterization result shows that the maximum roughness of the thin film samples after sulfurization. (d) Optical image of the WS_2/MoS_2 heterojunction. (e-f) SHG and FWM images of WS_2/MoS_2 heterojunction. (g-i) Surface characterization of WS_2, MoS_2 and WS_2/MoS_2 heterojunction by SEM.

We perform HRTEM on the cross-section of the WS_2/MoS_2 heterostructure. The materials grown on a silicon wafer were cut by focus ion beam (FIB, FEI Helios G3) and characterized by HRTEM (Tecnan G20). The obvious delamination of heterojunction can be seen from Figure S3 (a), the Pt on the heterojunction is used for protecting the 2D materials from FIB. The

heterogeneous interface can be clearly seen in the middle of the WS_2/MoS_2 heterostructure. The thickness of the WS_2 and MoS_2 layers is about 5 nm and 7 nm, respectively.

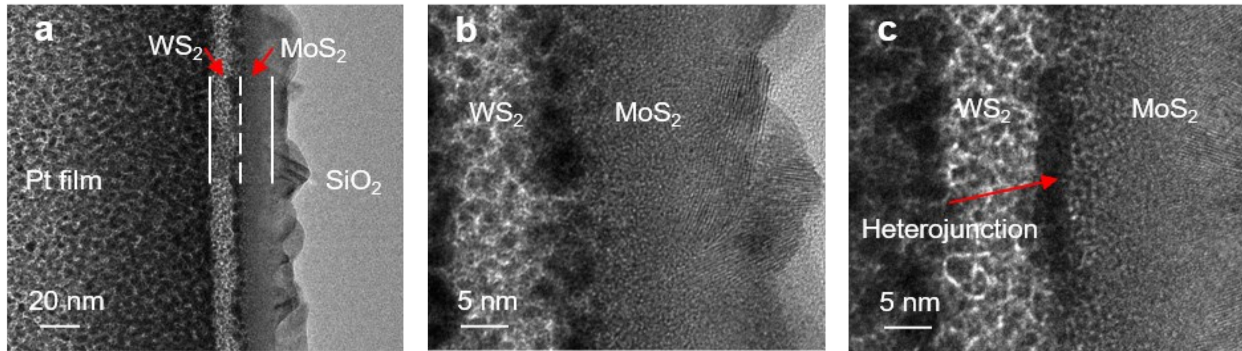

Figure S3 HRTEM images of the cross-section of WS_2/MoS_2 heterostructure growth on a Si/SiO_2 substrate. (a-c) Obvious layered WS_2/MoS_2 heterostructure, the Pt is coated to protect the 2D material from the FIB.

The WS_2/MoS_2 heterojunction was characterized by Raman spectroscopy with 514.5 nm laser (Renishaw InVia Raman microscope). Surface morphologies of heterojunction were characterized by field-emission scanning electron microscopy (Nova NanoSEM 450, 10kV). The thickness was detected by an atomic force microscope (Veeco NanoScope MultMode).

3. Typical I-V characteristics of the MoS2 and WS2 memristors

Figure S3a shows the schematic illustration of the MoS_2 thin film memristor. Synthetic MoS_2 layers on ITO substrate were fabricated using the same sulfurization method as growing WS_2/MoS_2 heterojunction. DC electrical measurements were performed on this device. As shown in Figure S3b, we can obtain a typical memristive switching cycle (State I). But after several switching cycles, the resistance state of the MoS_2 memristor always stays unalterably LRS (State II). Figure S3c shows the schematic diagram to explain the failure mechanism of the MoS_2 thin film memristor based on the MIM structure. After several cycles of resistance switching (State I), the sulfur ions penetrated the entire MoS_2 thin film to form the conducting filaments which are difficult to restore back to the original HRS state due to the inevitable lattice damage of the MoS_2 film. Therefore, the MoS_2 device is in a long-term LRS (State II). All the *I-V* characterizations are performed by using an Agilent Kesight B1500A semiconductor parameter analyzer with a Cascade probe station at room temperature.

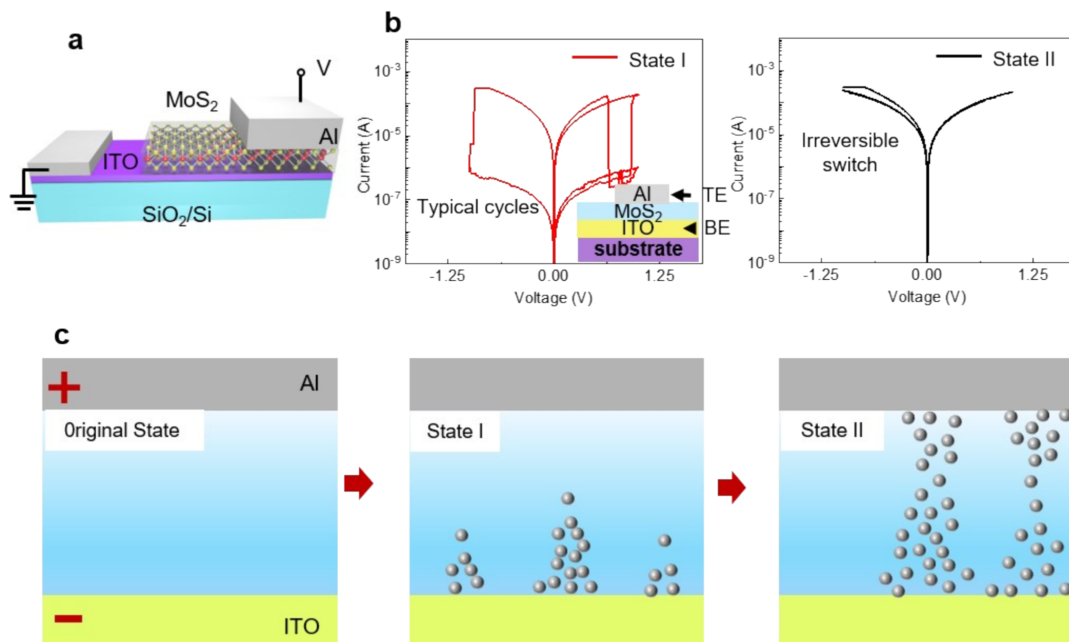

Figure S4. Typical *I-V* curves of the as-fabricated MoS_2 memristor. (a) Schematic diagram of the device structure of MoS_2 memristor. (b) Typical resistance switching curves of the MoS_2 memristor with respect to the applied voltage at the initial state (State I) and breakdown state (State II). (c) Schematic diagram of the failure mechanism of the conventional MIM MoS_2 memristor.

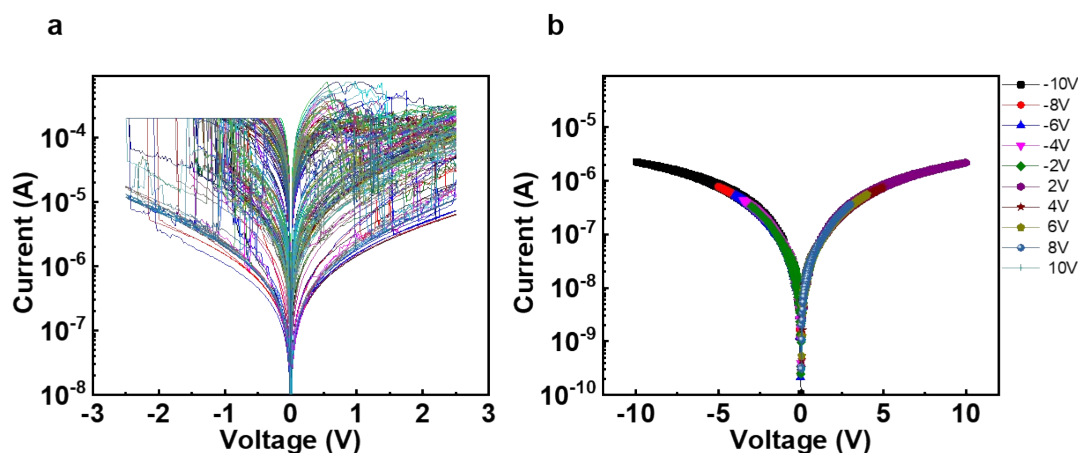

Figure S5. **(a)** Typical *I-V* switching curves of the Al/MoS_2/ITO memristor; **(b)** Typical *I-V* switching curves of the Al/WS_2/ITO memristor.

We have added one set of area-scaling experiments in the Supporting Information (Figure S6). The 2D material memristors with larger top electrodes are fabricated in the same way in

the control experiment. The inset of Figure S6 shows the schematic diagram of the devices. The resistance has a relatively uniform conductivity as revealed by the independent I-V characterization, which scales down a memristor cell with a resistance R_0 and area A_0 (100 μm × 100 μm), presenting in either low resistance state (LRS) or high resistance state (HRS). Moreover, the device with a larger electrode is demonstrated with their respective resistance R and area A (200 μm × 200 μm). For both states, a linear relationship $RA=a\ R_0A_0$ is obeyed by the chosen part. As shown in Figure S6, the value of the constant-coefficient a is close to 1, so the resistance of conducting layer is uniform under the applied voltages [Nanoscale, 8, 18113, (2016)]. This indicated a non-filamentary memristive mechanism, because if the filaments are formed in the localized spot, the resistance of the larger area could remain highly divergent to that of the surrounding function layer, then presenting orders of magnitude more resistive [Nature Electronics, 2, 66, (2019)].

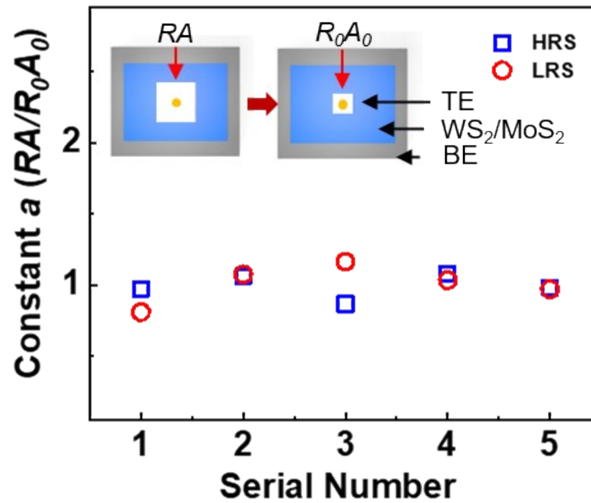

Figure S6. Area-dependent resistance measurement of featured heterojunction memristors: Range of constant a in the equation $RA=a\ R_0A_0$. Inset: schematic of the tested devices.

4. Influence of the sulfur ion distribution on the band structure and electrical conductivity of the WS_2/MoS_2 heterojunction

In order to study the influence of sulfur ion on the band structure and electric conductivity of WS_2/MoS_2 heterojunction, the thermionic emission theory was employed to figure out the relationship between the current flow across the heterojunction and the sulfur ions distribution.

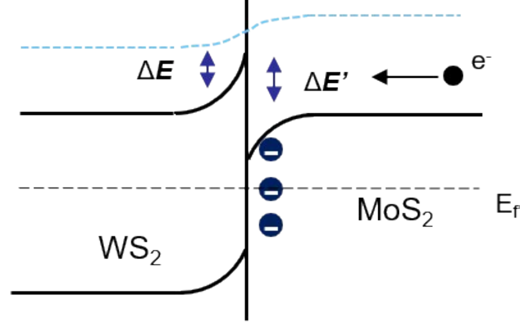

Figure S7: Band structure of the WS_2/MoS_2 heterojunction

According to Poisson's equation, the impurity concentration and potential relationship can be obtained as:

$$\frac{\exp\left(\frac{q}{k_B T}\varphi_1\right) - \frac{q}{k_B T}\varphi_1 - 1}{\exp\left(-\frac{q}{k_B T}\varphi_2\right) + \frac{q}{k_B T}\varphi_2 - 1} = \frac{\varepsilon_2 N_2}{\varepsilon_1 N_1} \tag{1}$$

where ϕ_1 and ϕ_2 are the barrier height of WS_2 and MoS_2 respectively. N_1 and N_2 are the net excess density near the contact, ε_1 and ε_2 are the dielectric constants of WS_2 and MoS_2. and kB is the Boltzmann constant. According to the thermal electron emission model, the formation of electron current is realized by diffusion motion. The effective electrons striking the wall of the barrier in a unit of time are only a part. The transmission coefficient X from Anderson's rules is applied to consider the electron reflection at the MoS_2/WS_2 interface. We assume the voltages applied on WS_2 and MoS_2 are V_1 and V_2, respectively. Then, we can obtain the equation of current density across the MoS_2/WS_2 heterojunction as follows:

$$J = XeN_2\sqrt{\frac{k_B T}{2\pi m}}\exp\left(-\frac{\varphi_2}{k_B T}\right) \times \left[\exp\left(\frac{eV_2}{k_B T}\right) - \exp\left(-\frac{eV_1}{k_B T}\right)\right] \tag{2}$$

where T is the temperature respectively. J is the thermionic emission current caused by the thermal motion of electrons. When V is a positive number, the second item in parentheses can be ignored. Then the equation (2) can be simplified to:

$$J = XeN_2\sqrt{\frac{k_B T}{2\pi m}}\exp\left(-\frac{\varphi_2}{k_B T}\right) \times \left[\exp\left(\frac{eV_2}{k_B T}\right)\right] \tag{3}$$

It is noted that there is also the presence of tunneling current in the heterojunction. Band structure variation with the change of electric field during the SET and RESET processes can be clearly reflected in Fig. 5(b).

According to the above equation, we can see that when the external voltage is increased, the partial pressure on both sides of the heterojunction is basically unchanged. As the voltage reaches the electric migration threshold of the sulfur ions, the sulfur ions rapidly aggregate at the MoS_2/WS_2 interface region on the MoS_2 side, causing a sudden increase in the effective impurity concentration. At the same time, the localized aggregation of sulfur ions causes an increase in tunneling probability, and hence the tunneling current is abruptly increased. Therefore, the current across the MoS_2/WS_2 heterojunction jumps at the SET process. Similarly, when a reverse voltage is applied, as the voltage reaches the migration threshold, and the sulfur ions are removed from the heterojunction region, thereby resulting in the decrease of the device current at the RESET process.

REFERENCES

1. Kresse, G.; Furthmüller, J., Efficient iterative schemes for ab initio total-energy calculations using a plane-wave basis set. Phys. Rev. B. **1996**, 54(16), 11169-11186.

2. Perdew, J. P.; Burke, K.; Ernzerhof, M., Generalized Gradient Approximation Made Simple. *Phys. Rev. Lett.* **1996,** 77(18), 3865-3868

3. Grimme S, Antony J, Ehrlich S, et al. A consistent and accurate ab initio parametrization of density functional dispersion correction (DFT-D) for the 94 elements H-Pu. The Journal of chemical physics, **2010**, 132(15): 154104.